

Numerical Methods for Studying Compressed Magnetic Field Generators

JOHN R. FREEMAN

Plasma Theory Division, Sandia Laboratories, Albuquerque, New Mexico 87115

AND

SAMUEL L. THOMPSON

*Computational Physics and Mechanics Division II,
Sandia Laboratories, Albuquerque, New Mexico 87115*

Received October 29, 1976

Explosively driven compressed magnetic field (CMF) power supplies have been used for a variety of applications. A two-dimensional MHD computational model, entitled COMAG, has been constructed to study the characteristics of helically wound CMF generators. The code combines an existing Eulerian materials response code with a two-dimensional (2D) magnetic field solver to compute the self-consistent interaction between the field and the conductors, including magnetic forces, Joule heating, and nonlinear resistive diffusion. Sample results are presented.

I. INTRODUCTION

Explosively driven compressed magnetic field (CMF) power supplies provide compact inexpensive generators of high current (megamperes), high energy (megajoules), and short current risetime (microseconds). Applications of these generators in plasma, solid-state, particle, and optical physics research have been reviewed by Knoepfel [1] and Fowler [2].

Helically wound generators, described by Shearer *et al.* [3] and Crawford and Damerow [4], have the advantage of a high initial inductance, permitting a potentially high amplification factor. Figure 1 shows a sketch of a typical generator. An initial pulsed current in the outer helical coil winding establishes magnetic flux between the coil and the inner metallic cylinder, referred to as the armature. The armature contains high explosive, which is detonated from one end, driving the armature towards the coil at high velocity. This action compresses the initial magnetic flux, leading to an amplification of the electrical current which can be delivered to an external load. The entire process converts chemical energy stored in the explosive into electrical energy delivered to the load.

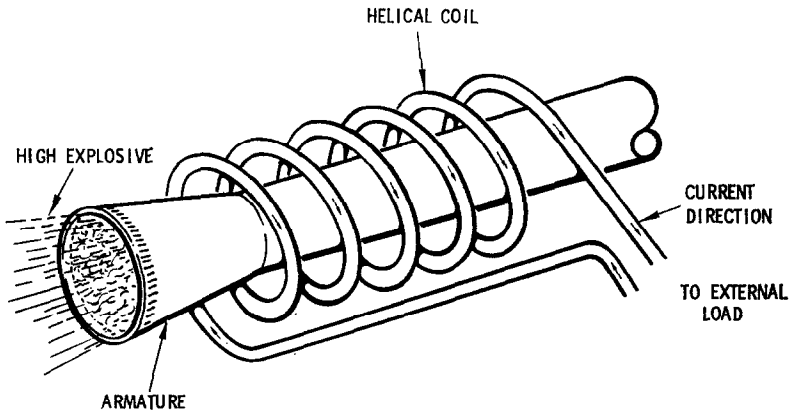


FIG. 1. Simplified CMF generator.

Calculations described in the preceding references and in other recent work [5-7] have separately examined various elements of the generator behavior, always in a one-dimensional approximation. This work describes a two-dimensional MHD model (entitled COMAG) used to study helically wound CMF generators. The model includes a complete mechanical response description using the CSQ finite difference hydrodynamic code [8]. The modifications necessary for this application are given in Section II as are methods of coupling the material response and magnetic field solver.

A two-dimensional finite difference magnetic field solver has been developed to treat the flux compression and the nonlinear temperature-dependent resistive diffusion into both conductors. The field solver has been coupled self-consistently to the hydrocode to properly include magnetic forces and Joule heating. The final element of the code is a circuit equation used to describe the self-consistent interaction between the generator and the external load. The circuit model retains an important feature of the helical coil, namely, the constancy of the total current in each loop of the coil.

The initial development of the code, plus a number of comparisons with analytic test cases, has been reported elsewhere [9, 10]. Section III of this work briefly summarizes all elements related to the field solver. Section IV discusses the choice of the computational mesh, while the boundary conditions are addressed in Section V. The relation of the generator inductance and resistance to the field quantities is described in Section VI. Section VII is concerned with details of the numerical methods for solving the field equations, with sample results summarized in Section VIII.

II. MECHANICAL RESPONSE/CSQ MODIFICATIONS

CSQ is a two-dimensional hydrodynamic program with energy flow and material strength. Extensive descriptions of the program are available [8]. The code has been widely used at a number of laboratories for a variety of calculations.

CSQ employs the finite difference analogs of the Lagrangian equations of motion (a material-fixed coordinate system) with a continuous rezoning to a space-fixed Eulerian coordinate system. Material strength effects, such as elastic-plastic behavior and fracture behavior are treated. An energy flow calculation includes radiation and various forms of thermal conduction. Realistic material descriptions with material phase transitions (solid-liquid, liquid-vapor, solid-solid, etc.) are available [11]. Various high explosive and other energy sources are included. Many of these features are necessary for proper description of the CMF generators.

The program has several other features which proved useful for the present application. CSQ was built with variable finite difference cell storage. The number of cell variables is adjusted to fit the present calculation. This means that no extensive modifications were required for storage of magnetic field quantities, current densities, etc. All restart, data editors, and plot programs work without modifications. This includes plots of the new quantities.

Another feature of CSQ that is of importance to the present problem is the size of the finite difference mesh which it can consider. Very marginal zoning for the problem under consideration requires a two-dimensional (2D) mesh of more than 100×100 – 10^4 cells. (The following calculations used somewhat more.) If 19 variables are stored for each cell, there are 1.9×10^5 ($=563060_8$) required words of storage. More accurate zoning can easily increase this number by a factor of 2 to 5. Arrays of this size are too large for the fast memory on available computers, so that larger (and slower) memories must be used. For efficient solutions of the magnetic field properties, both row and column access to the arrays is necessary. The CSQ storage procedure has the random-access feature built in. Any other method of storage (i.e., a sequential tape file or disk file) would force a completely different procedure of solution of the field equations or an inefficient program.

An Eulerian code has several advantages for this application. If a program with a Lagrangian mesh were used, severe mesh distortion would occur in the high explosive material and in the region of the contact of the armature and coil. This would necessitate frequent rezones of the Lagrangian mesh, a task which is both time consuming and undesirable. A second difficulty is that a Lagrangian mesh normally puts cells only in the materials. No mesh would exist in void regions, which can, of course, contain magnetic fields. This would force the use of a mesh continuation or separate mesh to treat the field properties.

CSQ can work in either rectangular or cylindrical coordinates. In the present situation, only cylindrical coordinates will be considered. The notation is changed from [8] to reflect this feature in more standard notation (r = radial coordinates; z = axial coordinates; θ = azimuthal coordinates). The Lagrangian forms of the conservation laws which control two-dimensional material motion (rotational symmetry) with independent energy flow and in the presence of magnetic field and currents are

conservation of mass,

$$\partial\rho/\partial t = -\rho\nabla \cdot \mathbf{V}; \quad (1)$$

conservation of momentum,

$$\rho \frac{\partial V_r}{\partial t} = - \frac{\partial}{\partial r} (\sigma_{rr} + Q_{rr}) - \frac{\partial \sigma_{rz}}{\partial z} - \frac{\sigma_{rr} - \sigma_{\theta\theta}}{r} + 0.1 (\mathbf{J} \times \mathbf{B})_r, \quad (2)$$

$$\rho \frac{\partial V_z}{\partial t} = - \frac{\partial}{\partial z} (\sigma_{zz} + Q_{zz}) - \frac{1}{r} \frac{\partial}{\partial r} (r\sigma_{rz}) + 0.1 (\mathbf{J} \times \mathbf{B})_z; \quad (3)$$

and conservation of energy,

$$\frac{\partial E_m}{\partial t} = - \frac{1}{\rho} \text{tr}\{(\sigma + Q) \cdot D\} - \frac{1}{\rho} \nabla \cdot \mathbf{F} + \mathcal{E} + \frac{10^7}{\rho\sigma_c} (\mathbf{J} \cdot \mathbf{J}); \quad (4)$$

where all quantities are defined in the following list. The thermodynamic and mechanical units are cgs. Practical cgs units are used for the electromagnetic quantities (J has units A/cm², σ_c has units Ω^{-1} /cm, B has units G). The notation will be as follows, except as noted in the text:

- ρ = density (g/cm³),
- t = time (sec),
- \mathbf{V} = velocity vector (cm/sec),
- E_m = specific material internal energy (erg/g),
- σ = stress tensor (dyn/cm²),
- D = stretching tensor (sec⁻¹),
- Q = viscosity tensor (dyn/cm²),

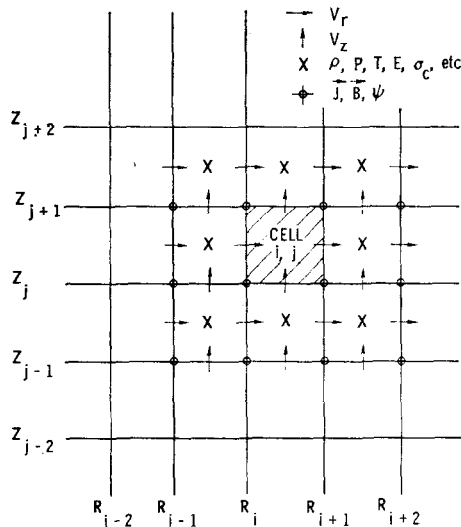


FIG. 2. Placement of variables in finite difference mesh.

- \mathbf{F} = energy flow flux vector (erg/cm² sec),
 $\dot{\mathcal{E}}$ = specific internal energy production rate (erg/cm sec),
 \mathbf{J} = current density (A/cm²),
 \mathbf{B} = magnetic field intensity (G),
 σ_c = electrical conductivity (Ω^{-1} /cm).

The inclusion of the \mathbf{J} and \mathbf{B} terms in the CSQ finite difference relations is straightforward. The placement of variables in the finite difference mesh is shown in Fig. 2. This method works well and requires little interpolation of variables within the grid. Other details of the difference method are available in [8].

III. THE MAGNETIC FIELD SOLVER

Figure 3 shows a cross section of the computational region defined for the model. All three-dimensional effects are omitted, and a cylindrically symmetric region is considered. A further approximation made is to neglect coil motion in the field solver. Earlier studies performed without this approximation indicated that significant coil expansion occurred only after the armature contacted the coil. Motion of the coil after that time had no effect on the field generation. Because the explosive is detonated from only one end, the armature makes initial contact with the coil at that end. This point of contact then sweeps up the coil, effectively shorting the helical turns together. This decrease in the coil inductance is one of the sources of current amplification, the remaining one being the inductance decrease due to the reduction in cross-sectional area of the vacuum region between the coil and armature. As the point of

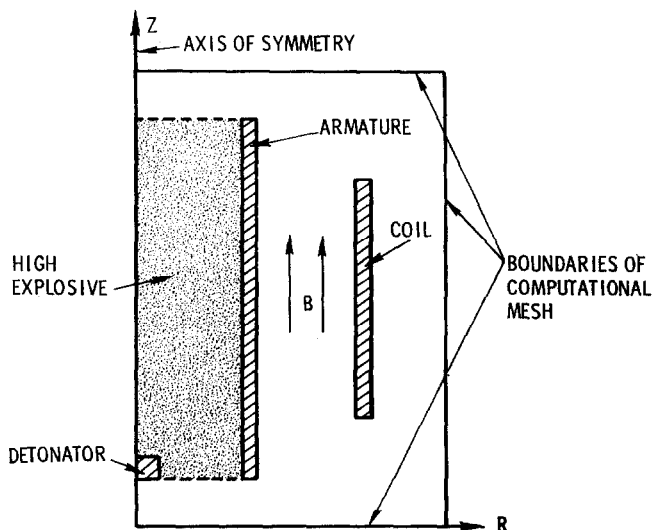


FIG. 3. Computational region.

contact between the armature and coil sweeps up the generator, the region of computation of the magnetic fields is also adjusted in phase. No field calculations take place in the conductors in axial regions below the point of contact, primarily because these regions are decoupled by the turns shorting and do not affect the generator performance. None of these approximations apply to the motion calculations of CSQ. The limitations here are used only in the field solver.

We write Maxwell's equations as (using practical cgs units)

$$\nabla \times \mathbf{E} = -10^{-9}(\partial \mathbf{B} / \partial t), \quad (5)$$

$$\nabla \times \mathbf{H} = 0.4\pi \mathbf{J}, \quad (6)$$

where the displacement current has been neglected. In the two conductors, we have as Ohm's law

$$\mathbf{J} = \sigma_c[\mathbf{E} + 10^{-8}(\mathbf{V} \times \mathbf{B})]. \quad (7)$$

Equations (5)–(7) can be combined with the definitions $\mathbf{E} = -10^{-8} \partial \mathbf{A} / \partial t$, $\mathbf{H} = \mathbf{B}$ (free-space permeability), and $\nabla \times \mathbf{A} = \mathbf{H}$ to yield,

$$\frac{\partial \Psi}{\partial t} = \kappa_0 \left(\frac{\partial^2 \Psi}{\partial r^2} + \frac{\partial^2 \Psi}{\partial z^2} \right) - \left(V_r + \frac{\kappa_0}{r} \right) \frac{\partial \Psi}{\partial r} - V_z \frac{\partial \Psi}{\partial z}, \quad (8)$$

where $\Psi = rA_\theta$ is the magnetic stream function, A_θ is the vector potential, and $\kappa_0 = 10^9/4\pi\sigma_c$ is the magnetic diffusivity. In the vacuum regions surrounding the conductors, we have

$$\frac{\partial^2 \Psi}{\partial r^2} - \frac{1}{r} \frac{\partial \Psi}{\partial r} + \frac{\partial^2 \Psi}{\partial z^2} = 0. \quad (9)$$

The components of the magnetic field are given by

$$H_z = \frac{1}{r} \frac{\partial \Psi}{\partial r}, \quad H_r = -\frac{1}{r} \frac{\partial \Psi}{\partial z}. \quad (10)$$

The initial studies reported used Eq. (8) in both the coil and armature and Eq. (9) for the vacuum region [9, 10]. This turned out to be disadvantageous when the circuit equation was added. It was found to be extremely difficult to enforce the helicity requirement (the constancy of the total current in each coil loop) using the stream function definition in the coil. The reason for this is the inductive coupling between the coil turns. The stream function at any specific coil loop location consists of contributions from itself, plus all remaining turns. It thus is quite difficult (without using a large inductance matrix) to specify boundary conditions on the stream function which would yield equal total currents in all coil loops.

Because of this difficulty, a new model for the coil was derived, based on the current density rather than the stream function. The sequence of operations is as follows:

1. Begin with an initial current density distribution J_0 in the coil at an initial time t_0 ; also begin with an initial stream function definition Ψ everywhere in the

computational region, including the coil, consistent with both the boundary conditions and the initial coil current densities. This is obtained by solving the equation

$$\frac{\partial^2 \Psi}{\partial r^2} - \frac{1}{r} \frac{\partial \Psi}{\partial r} + \frac{\partial^2 \Psi}{\partial z^2} = -0.4\pi rJ, \quad (11)$$

instead of Eq. (9). Compute the stream function on all boundaries in terms of the analytic elliptic integral formulation (Section V).

2. Begin the actual time advancement by diffusing the current densities in the coil, using

$$\frac{\partial J}{\partial t} = \kappa_0 \left[\frac{\partial^2 J}{\partial r^2} + \frac{1}{r} \frac{\partial J}{\partial r} - \frac{J}{r^2} \right], \quad (12)$$

where the axial diffusion is omitted because of electrical insulation between coil turns. (Equation (12) neglects spatial variations in the electrical conductivity.)

3. Compute the stream function in the armature using Eq. (8).

4. Compute predicted (first-order linear extrapolation in time) coil circuit total current I_p (equal for all coil loops).

5. Adjust magnitudes of all diffused coil current densities consistent with the predicted total coil current. This is done by multiplying the current densities determined in step 2 by the ratio I_p/I_i , where I_i is the total current in each loop at the end of step 2.

6. Obtain predicted stream function everywhere, using Eq. (11). (The stream function in the armature region is already computed by step 3 and must be held fixed during this step, i.e., the computed values of the stream function in the armature are treated as boundary conditions when integrating Eq. (11).) Recompute the boundary conditions (Section V) at the start of this step, using the coil currents of step 5 and the armature currents of step 3.

7. Define coil inductance and resistance in terms of the predicted stream function and compute a *corrected* coil current at t^{n+1} , the new time level, using the circuit equation (including the external load impedance). Adjust coil current density magnitudes consistent with the corrected total current.

8. Compare predicted and corrected current values; if they differ by more than a few percent, repeat step 6 to obtain the corrected stream function everywhere. Check boundary stream functions for convergence; return to step 6 if unconverged.

The preceding sequence of operations (from step 2 through step 8) is performed at each time step of the calculation. The procedure is most simply stated to be an iteration on the coil circuit current and the boundary conditions (determined in terms of the internal current distribution) such that at each time level a completely self-consistent time-centered solution is achieved. In the converged state the stream function everywhere, including the boundaries, is consistent with the current density distribution throughout the mesh. At the same time, the total circuit current is consistent with

the inductance and resistance (Section VI) determined from the field distribution. At the beginning of each step, the hydrodynamic portion of the code supplies the armature location, the velocity distribution in the armature, and conductor temperatures to compute σ_c . At the end of each time step, the field solver stores the magnetic fields and currents to be used in both conductors at the next hydro time step.

IV. THE COMPUTATIONAL MESH

One of the principal difficulties of this application is spatial resolution of the small skin depths in the armature and the coil. These skin depths are typically very small, on the order of a few percent of the coil radius. A uniform spatial difference mesh typically requires between 100–200 zones in each direction to even minimally provide this resolution.

The magnetic field solver and the hydrodynamics portion of the code use the same basic Eulerian mesh, with the field quantities defined at the mesh corners as shown in Fig. 2. Some improvement in spatial resolution was achieved by using unequally spaced zones in the radial direction. The axial mesh was chosen equal to the coil turn spacing, thereby precluding any study of axial diffusion in the coil turns or proximity effects between loops. Inasmuch as the coils considered were wound at a constant pitch, this resulted in uniform axial zones.

V. BOUNDARY CONDITIONS

Solution of Eq. (11) over the region of computation requires boundary conditions on the stream function. Because of cylindrical symmetry, $\Psi(0, z) = 0$ at the axis of symmetry. The previously reported computations employed Neumann boundary conditions elsewhere, with $\partial\Psi/\partial z = H_r = 0$ at the two axial boundaries and $\partial\Psi/\partial r = H_z = 0$ at the outer radius [9, 10]. These boundary conditions are appropriate for conductors which are long compared with their radii. Inasmuch as the cases studied violated this condition, errors resulted in the inductance calculation. The computed generator inductance was typically about 25% high when compared with experimental values.

More recent calculations have been performed which take proper account of the fringing fields at the boundaries of the generator. This is done by evaluating the analytic solution for the stream function of the current loops, obtaining the correct boundary value by summing the contributions from all the internal current loops. Finite pitch effects of the helix are omitted in this treatment.

Consider a point on the boundary given by the coordinates (r, z) . Let a particular current loop (in either the coil or the armature) be located at (r_c, z_c) . From Smythe [12] the magnetic stream function at the point (r, z) produced by a current loop of magnitude I located at (r_c, z_c) is

$$\Psi(r, z) = 0.2 I r [(1 + \bar{r})^2 + \bar{z}^2]^{1/2} [(1 - k^2/2) K - E], \quad (13)$$

where $\bar{r} = r_c/r$, $\bar{z} = (z - z_c)/r$, $k^2 = 4\bar{r}/[(1 + \bar{r})^2 + \bar{z}^2]$, and K and E are the complete elliptic integrals of the first and second kind, of the argument k .

Prior to each time step in the field calculation, the stream function at both axial boundaries and the outer radial boundary is computed by summing contributions of the form given by Eq. (13) over all interior current loops. This yields a fringing field distribution consistent with the boundary condition $\Psi \rightarrow 0$ as $r, z \rightarrow \infty$. It was necessary to include the boundary condition computation in the major iteration loop to ensure, as indicated in Eq. (13), that the loop currents I and the boundary values of Ψ were fully self-consistent. The use of these boundary conditions reduced the error in the inductance calculation to only a few percent. Prestoring the geometric factors which were invariant in time permitted this treatment to be employed with a negligible decrease in computational speed. Similar treatments have been used in other 2D MHD work [13] and in recent calculations of electron ring accelerator behavior [14].

VI. GENERATOR INDUCTANCE AND RESISTANCE

A circuit diagram of the generator and load is shown in Fig. 4. The charging source is used to establish the initial current. At the desired level, the charging circuit is explosively switched out of the circuit by the shorting switch. The current I_c in the coil circuit is then governed by

$$d/dt (L_T I_c) + R_T I_c = -\dot{\Psi}_L, \quad (14)$$

where the total circuit inductance L_T consists of L_L , the load inductance, plus L_c , the generator inductance. The total resistance R_T is the sum of R_L , the load resistance, plus R_c , the coil resistance. The loss term $\dot{\Psi}_L$ represents the diffused flux switched out of the load circuit by the moving contact between the armature and the coil [1, 3, 4]. We obtain the generator inductance from the magnetic stream function by equating the lumped-parameter field energy definition to the computed value

$$\frac{1}{2} L_c I_c^2 = \frac{1}{2} \left(\sum_i \Psi_i I_i \right) 2\pi \times 10^{-8}, \quad (15)$$

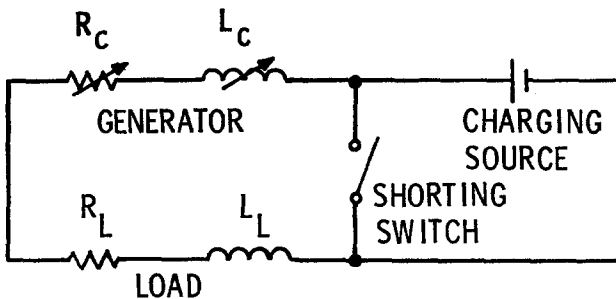


FIG. 4. CMF generator circuit.

where the right-hand side of Eq. (15) is summed over all loops of the coil. Since the current I_i in the helical coil is constant and equal to I_c for all loops, we have that

$$L_c = \left(\sum_i \Psi_i / I_c \right) 2\pi \times 10^{-8} \text{ H.} \quad (16)$$

The coil resistance R_c is similarly obtained by equating the lumped-parameter coil dissipation with the computed value,

$$I_c^2 R_c = \int J^2 / \sigma_c dV, \quad (17)$$

where dV is the volume element, $dV = 2\pi r dr dz$. Since each coil turn has an axial width Δz and a radial thickness of a number of zones, we have

$$R_c = \sum_i \left[\int \frac{J^2 r dr}{\sigma_c} \right]_i \frac{2\pi \Delta z}{I_c^2}, \quad (18)$$

where the integral in Eq. (18) is numerically evaluated for each coil loop, and the summation extends over all loops, representing the fact that the turns can be considered to be connected in series.

The flux loss term Ψ_L due to flux diffusion into the coil, Ψ_{L_c} , and the armature, Ψ_{L_a} , is given by $\Psi_L = \sum_j \Psi_{L_a} / \Delta t + \sum_j \Psi_{L_c} / \Delta t$, where the summation extends only over the coil turns and armature length shorted between time t and $t + \Delta t$.

VII. NUMERICAL METHODS FOR THE FIELD SOLVER

At each time step, it is necessary to solve two basic equations for the stream function, namely, Eq. (8) in the armature and Eq. (11) elsewhere. Equation (8) is integrated in time using the explicit flux-corrected transport method of Boris and Book [15]. A time-splitting of the equation is performed, so that the first half of the time step is used to integrate the radial terms and the second half is used to integrate the axial terms. The difference equations for this procedure and a variety of comparisons with analytic test cases have been discussed previously [9, 10]. Recent modifications have generalized the difference equations for a variably spaced (but fixed) mesh.

It is necessary to obtain the solution of Eq. (11) for the stream function in the vacuum and coil regions. The second-order accurate difference equation for Eq. (11) is given by

$$-C_j \Psi_{j+1,l} + (2 + A_j + C_j) \Psi_{j,l} - A_j \Psi_{j-1,l} - (\Psi_{j,l+1} + \Psi_{j,l-1}) = F_{j,l}, \quad (19)$$

where

$$\begin{aligned} A_j &= (1 + \Delta^+/2r_j) \Delta z^2 / \Delta^- \Delta_{AV}, \\ C_j &= (1 - \Delta^-/2r_j) \Delta z^2 / \Delta^+ \Delta_{AV}, \\ \Delta^+ &= r_{j+1} - r_j, \\ \Delta^- &= r_j - r_{j-1}, \\ \Delta_{AV} &= (\Delta^+ + \Delta^-)/2, \\ F_{j,l} &= 0.4 \pi \Delta z^2 r_j J_{j,l}. \end{aligned}$$

Equation (19) is written assuming that the mesh is variably spaced in the radial direction, but uniform in the axial direction. The j -index refers to radial mesh points and the l -index refers to axial mesh points.

Equation (19) was solved by the alternating direction implicit (ADI) method using the parameter sequence of Wachspress [16]. The approach is an iterative method in which each iteration involves splitting Eq. (19) into two implicit substeps,

$$\begin{aligned} & -C_j \Psi_{j+1,l}^* + (A_j + C_j + \xi^n) \Psi_{j,l}^* - A_j \Psi_{j-1,l}^* \quad (20a) \\ & = \Psi_{j,l+1} - (2 - \xi^n) \Psi_{j,l} + \Psi_{j,l-1} + F_{j,l}, \end{aligned}$$

$$\begin{aligned} & -\Psi_{j,l+1}^n + (2 + \xi^n) \Psi_{j,l}^n - \Psi_{j,l-1}^n \\ & = C_j \Psi_{j+1,l}^* - (A_j + C_j - \xi^n) \Psi_{j,l}^* + A_j \Psi_{j-1,l}^* + F_{j,l}. \quad (20b) \end{aligned}$$

The convergence parameters ξ^n are varied at each iteration to improve convergence. The tridiagonal matrix Eqs. (20a) and (20b) are solved by an efficient two-pass direct method described by Richtmyer and Morton [17]. A six-parameter variation of ξ^n was used, given by

$$\xi^{n+1} = \frac{4 \cos^2 \pi/2m}{(\cot^2 \pi/2m)^{n/5}} \quad (n = 0, \dots, 5). \quad (21)$$

The parameter m was set equal to 100, the approximate number of meshes in each direction. The iteration parameter sequence was repeated after every six iterations. Convergence for a mesh of about 100×100 was obtained in about 25 iterations. The relative convergence criterion invoked was that the stream function at no mesh point varied by more than 10^{-4} of its absolute value from the final to the preceding iteration. The convergence obtained was about a factor of six faster than that with a constant convergence parameter ξ . As this portion of the field solver remains the most time-consuming, this improvement was critical in terms of overall program speed.

VIII. EXAMPLE CALCULATIONS

In this section the results of two COMAG calculations are given. The actual generator is the same for the two cases. The first case (L14) used a high inductance external load, while the second case (L15) used a low inductance load, relative to the

generator inductance. The initial conditions for the circuit properties are shown in Table I for both calculations.

The device configuration is shown in Fig. 5. The center line of the cylindrically symmetric system is at the left of Fig. 5. The coil winding is much more closely spaced than shown in Fig. 1; the pitch is approximately the same as the wire diameter and appears continuous on the plot. The coil is enclosed in a packing material, which is not shown in Fig. 1.

TABLE I
Initial Circuit Parameters

	L14	L15
Current (A)	220	220
Coil inductance (μH)	78.42	78.42
Load inductance (μH)	48.58	0.1
Coil resistance ^a (Ω)	1.12	1.12
Load resistance (Ω)	0.13	0.015

^a For uniform current distribution.

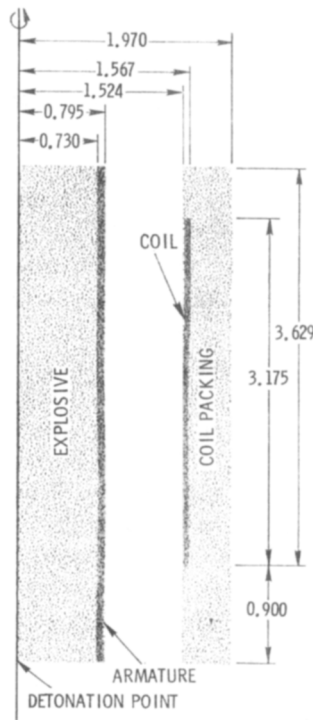


FIG. 5. Example of generator configuration.

The high explosive used was LX-04 with an initial density of 1.865 g/cm^3 , detonation velocity of $8.47 \times 10^5 \text{ cm/sec}$, and Chapman–Jouguet pressure of $3.4 \times 10^{11} \text{ dyn/cm}^2$. For this configuration $5.35 \mu \text{ sec}$ was required to complete the burn with an energy release of about $7.2 \times 10^{11} \text{ erg}$ [18]. Both the armature and coil were copper with an initial density of 8.94 g/cm^3 . The thermodynamic and elastic properties were as listed by Thompson [11]. The electrical conductivity properties were taken from Knoepfel [1].

The purpose of the coil packing material is to constrain the material after the armature–coil collision. In the experimental configuration it also served to hold the coil in place. The details of its material properties are not important to the calculations other than being sufficiently massive. Hence for reasons of economy, this material was taken to be the same as the explosive.

The zoning of these calculations is quite difficult. There are many conflicting requirements from the various computational sections and computer storage limitation. The following represents a compromise which attempts to satisfy the minimum requirements for each section and still fit the data into the CDC 7600. A constant spacing in the Z coordinate is used with a total of 100 meshes. There are 70 meshes within the length of the coil. The radial zoning is more complex with a total of 104 variably spaced meshes. The smallest meshes are 0.00839 cm near the coil, while the width near the armature is 0.013 cm , with a smooth variation between the coil and armature. Considerably larger meshes are used in the explosive and packing material regions. The total number of cells is then 1.04×10^4 . Each calculation required about 6.5 hr of central processor time on the CDC 7600.

The mechanical response for the L15 case is shown in the left half of Fig. 6a to 6e. The plots are produced with the reflection about $r = 0$. About $5 \mu \text{ sec}$ after the start of detonation, the first contact between the armature and the coil packing is made; the first contact of the armature and coil is at $5.75 \mu \text{ sec}$. The complete length of the coil is swept out by $8.76 \mu \text{ sec}$. The pressure at the impact surface is sufficiently high to yield considerable heating, but this occurs after the coil turn is removed from the circuit. Both the coil and armature remain well below the melting point while in the circuit for this configuration.

The computed field lines are shown on the right-hand sides of the figures. The conductors are outlined by asterisks. Figure 6a has the same field of view ($r - z$) as the material configuration plots. The field of view in the other figures is reduced in the radial coordinate for clarity as shown. The large increase in the magnetic field strength as the calculation proceeds forces a change in the scale for the plotted field lines. The two marked lines are at the same field strengths in all plots.

Figure 7 shows three-dimensional views of the stream function with the hidden sections of the surface removed. Both have the same scale and are plotted directly from the code output without smoothing. The lack of noise in the solution is evident. At the end of the calculation the Ψ scale would have to be changed by a factor of 10 for the surface to be shown in the same plot height.

The mechanical response is nearly identical for the two calculations L14 and L15. This implies that the magnetic terms in Eqs. (2) to (4) are not large relative to other

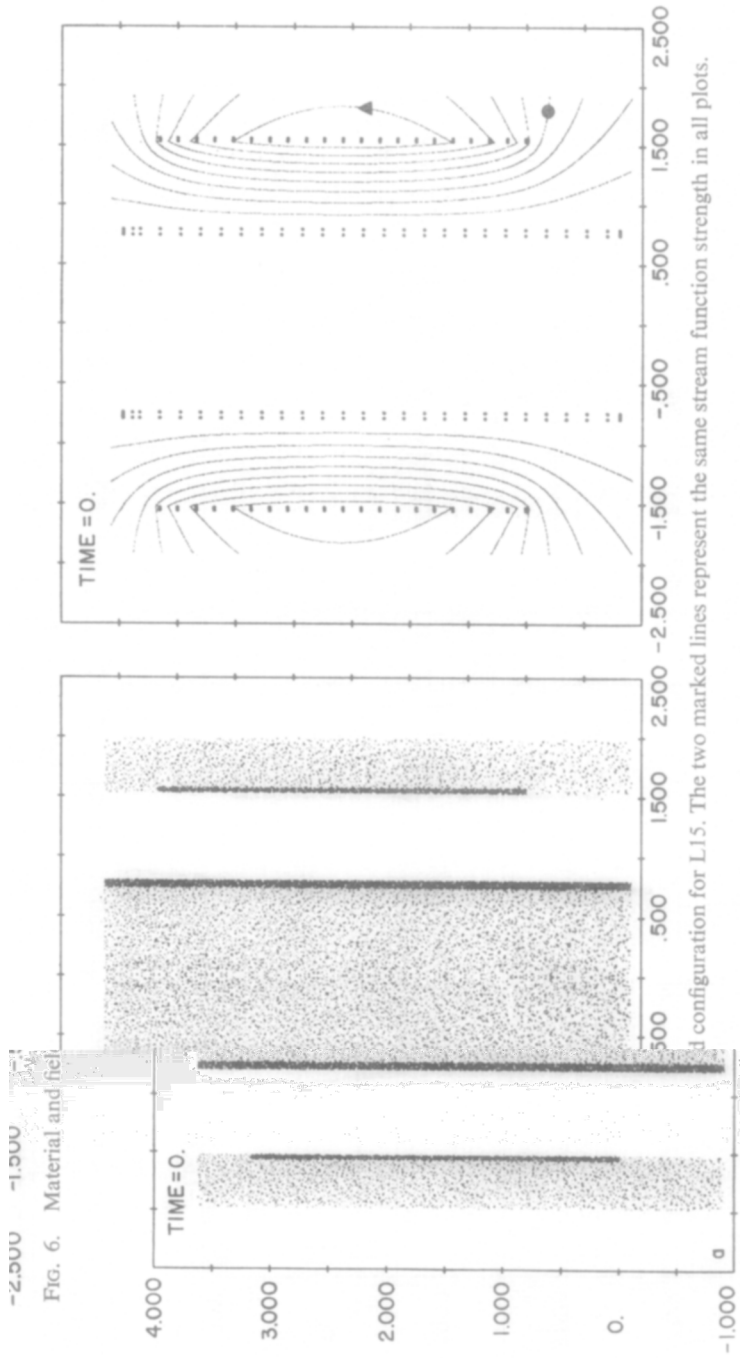
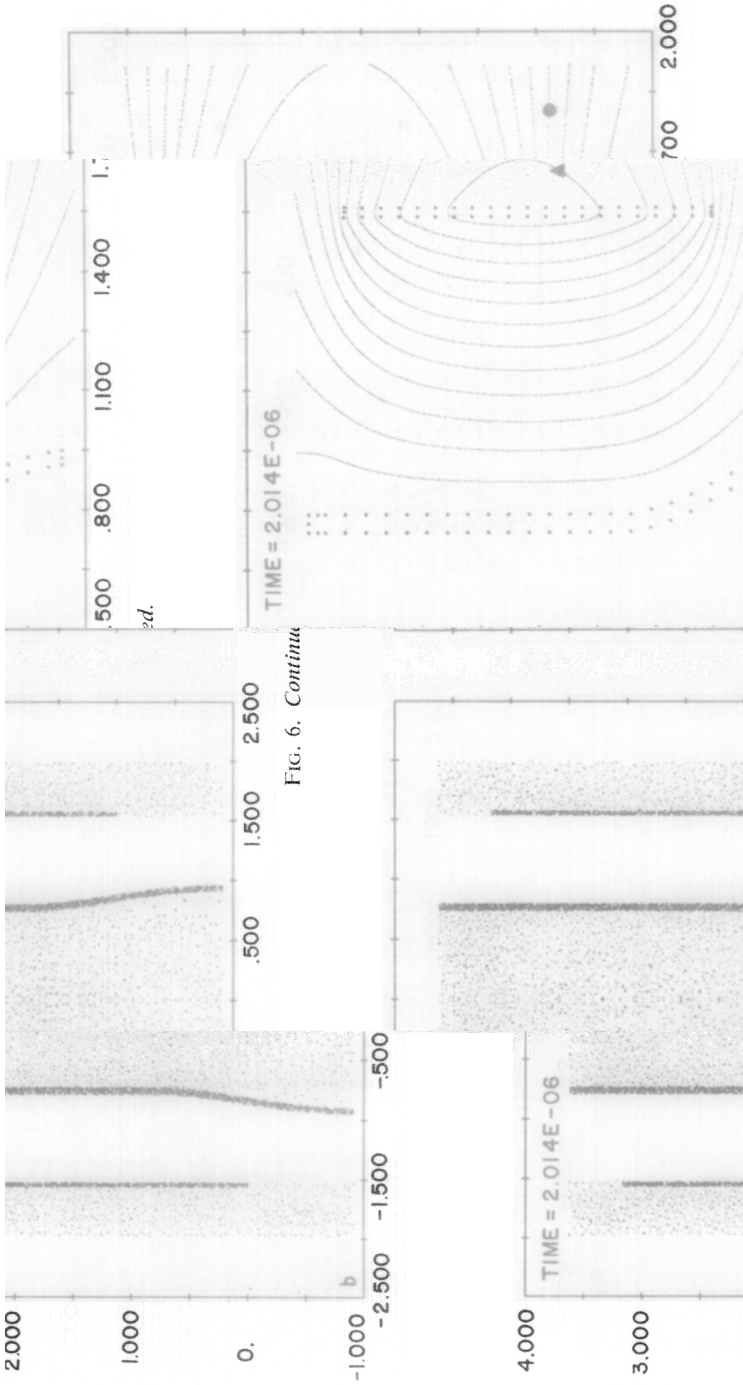
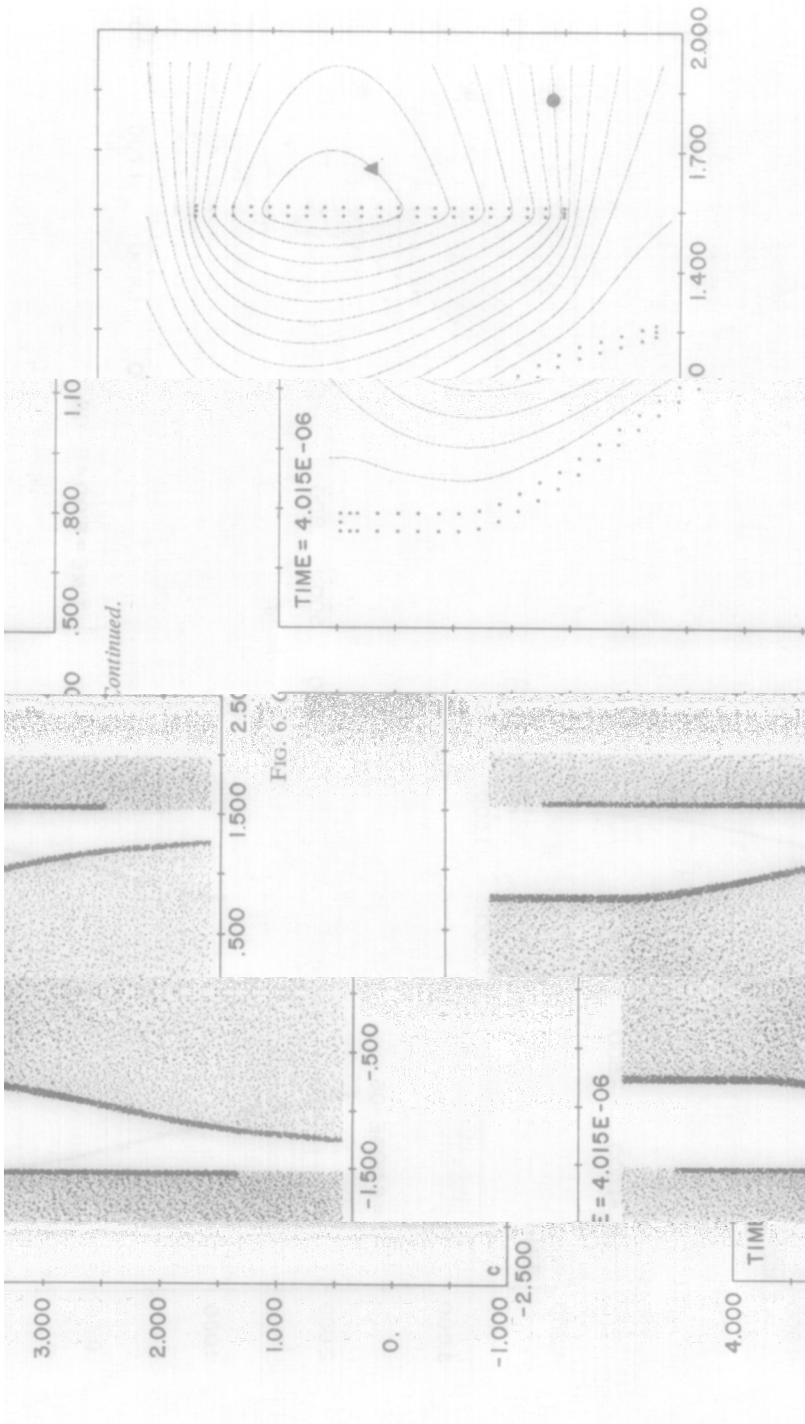
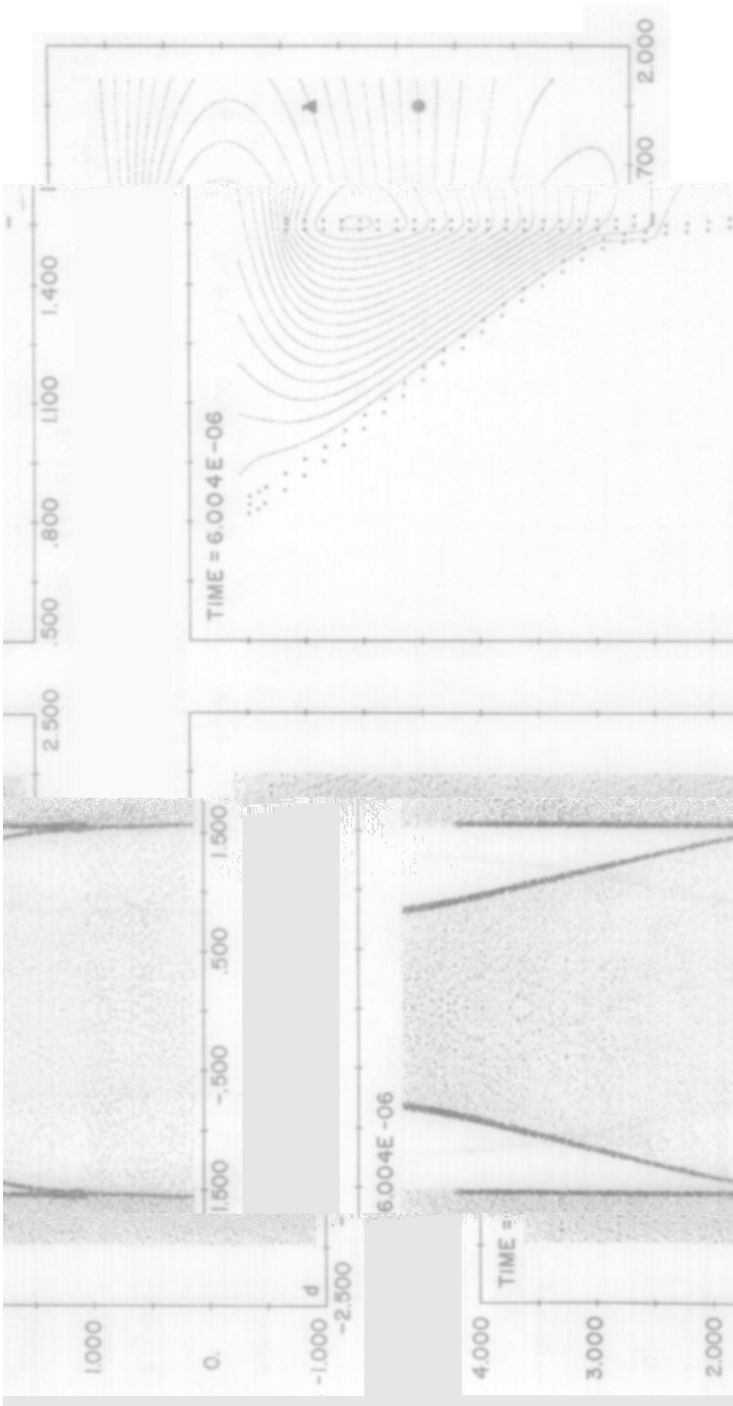


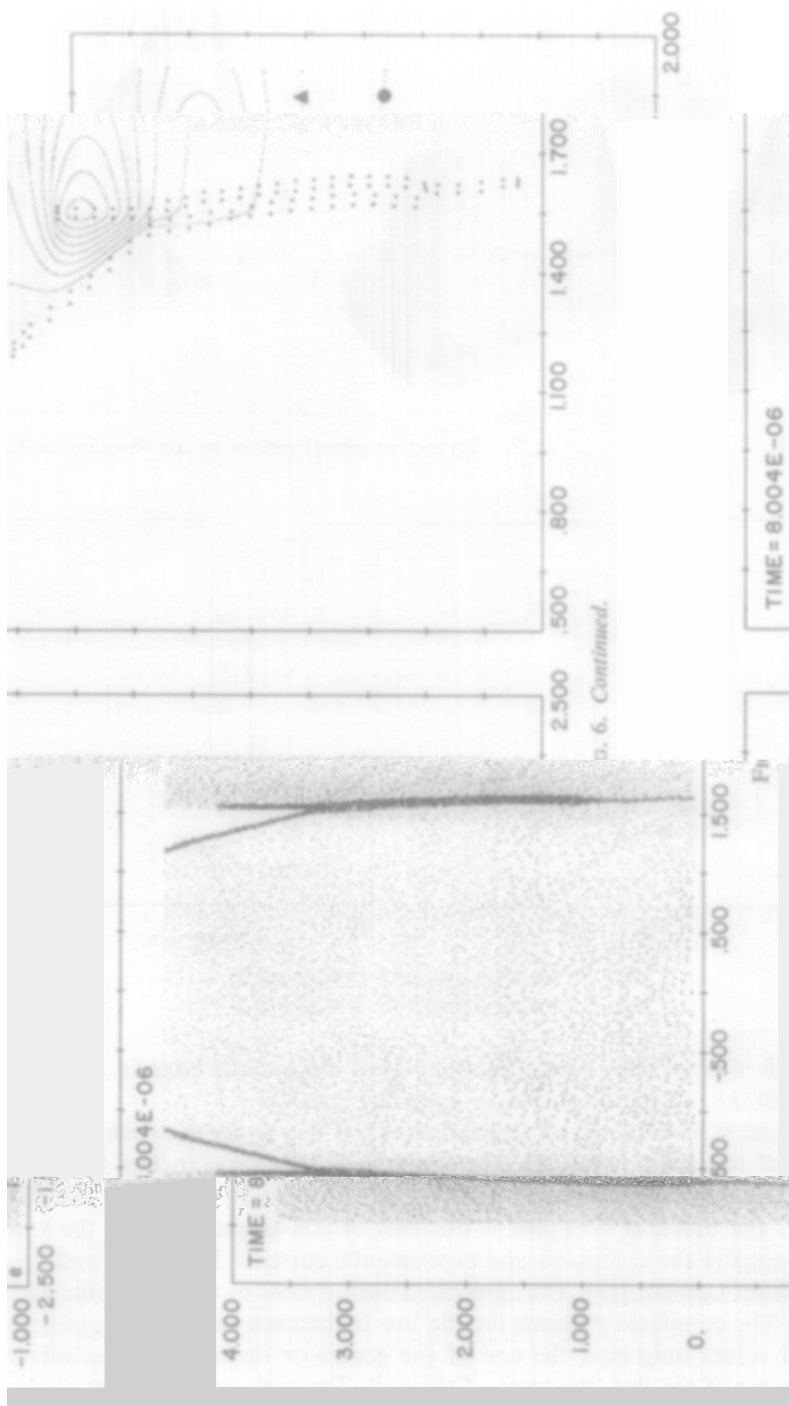
Fig. 6. Material and field

configuration for L15. The two marked lines represent the same stream function strength in all plots.









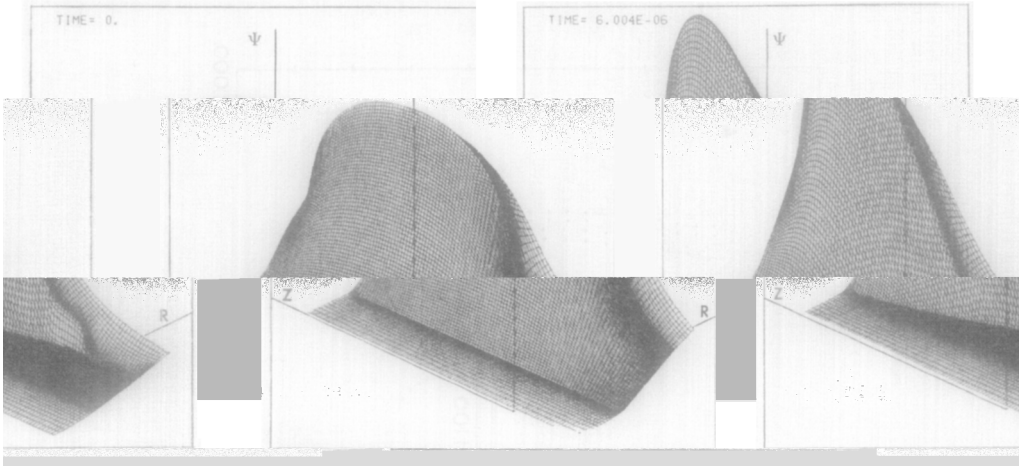


FIG. 7. Three-dimensional view of stream function for L15.

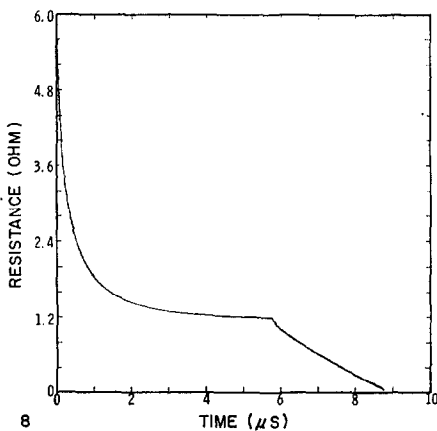


FIG. 8. Coil resistance for L14 and L15.

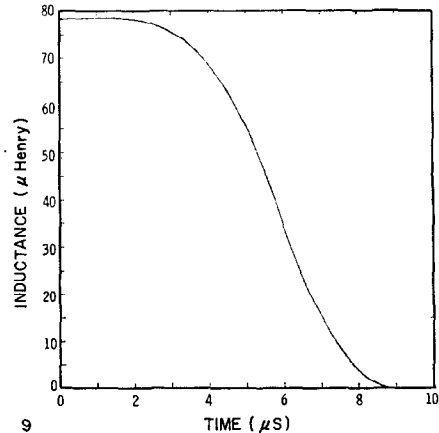


FIG. 9. Coil inductance for L14 and L15.

terms through most of the material motion. They did become large in L15 but only near the end of the calculation and for a very short time.

Figures 8 and 9 show the circuit characteristics of the device for both calculations. The static coil resistance is 1.12Ω . The initial resistance drop in Fig. 8 reflects the fact that the initial current was assumed to be a surface current which slowly diffused into the wire. The break at $5.75 \mu\text{sec}$ is the start of coil-armature shorting.

Figures 10 and 11 compare the computed and experimental currents. Experimental values were obtained from Leeman [19]. The agreement during most of the generator operation is excellent. The computed currents for the low inductance case are higher than the experimental values only near the end of the generator operation, a time corresponding to shorting of the last few turns of the coil. There are many possible

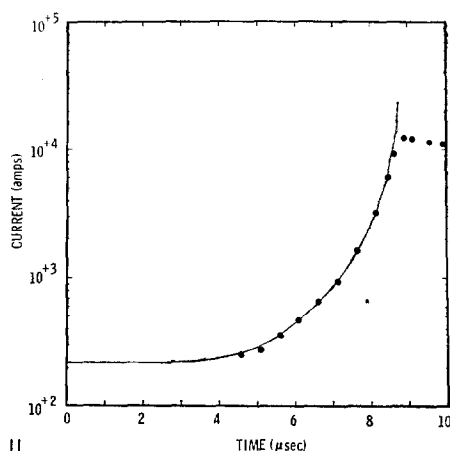
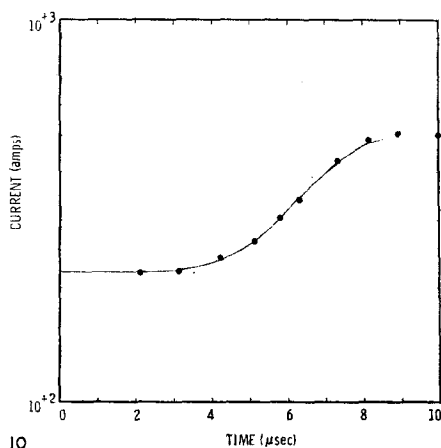


FIG. 10. Computed and experimental (●) currents for L14.

FIG. 11. Computed and experimental (●) currents for L15.

reasons for this disagreement including turn-to-turn electrical breakdown in the coil, delayed electrical shorting of the armature and coil caused by the insulating material, instabilities or three-dimensional behavior in armature expansion, venting of explosive gases into the region between the armature and coil, residual inductances of the generator output and return connections, and three-dimensional effects at the end of the generator where the helical coil couples to the output connectors. There are also only a few meshes in the region of computation important to the circuit properties. These and other effects are under study.

IX. CONCLUSIONS

We have described the construction of COMAG, a code designed to study CMF generators. The code provides a self-consistent 2D MHD description of the generator, including the effects of the external load.

Because of the complexity of the physical model, COMAG calculations are quite time-consuming, requiring hours of CDC 7600 time. These calculations will thus be of value in studying the details of important nonlinear physical effects, rather than being useful as a design tool. A recent report by Tucker and Leeman [20] describes a simplified lumped-parameter circuit model of the generator which runs in a few minutes on the CDC 6600. This code provides a capability for inexpensive design parameter variations, with the final designs selected to be studied using COMAG. In addition, the accuracy of the various lumped-parameter circuit approximations can be studied using COMAG. Finally, the numerical techniques described herein have applicability to a broad class of 2D MHD problems, including a study of advanced MHD generators [21] and magnetic field effects on electron beam fusion targets [22].

ACKNOWLEDGMENTS

The authors would like to acknowledge many helpful discussions with J. Gover and T. J. Tucker. The experimental data for Figs. 10 and 11 were provided by J. E. Leeman.

REFERENCES

1. H. KNOEPFEL, "Pulsed High Magnetic Fields," North-Holland, Amsterdam, 1970.
2. C. M. FOWLER, *Science* **180** (1973), 261.
3. J. W. SHEARER *et al.*, *J. Appl. Phys.* **39** (1968), 2102.
4. J. C. CRAWFORD AND R. A. DAMEROW, *J. Appl. Phys.* **39** (1968), 5224.
5. V. I. YURCHENKO, *Sov. Phys.-Tech. Phys.* **19** (1975), 1031.
6. L. S. GERASIMOV, *Sov. Phys.-Tech. Phys.* **19** (1975), 1226.
7. B. ANTONI, C. NAZET, AND L. POBE, Theoretical and Experimental Study of Explosive-Driven Magnetic Field Compression Generators, in "Proceedings of the International Conference on Energy Storage, Compression, and Switching," Plenum Press, New York, 1976.
8. S. L. THOMPSON, *CSQ—A Two-Dimensional Hydrodynamic Program with Energy Flow and Material Strength*, Sandia Laboratories Report SAND-74-0122, 1975.
9. J. R. FREEMAN AND S. L. THOMPSON, Two-Dimensional *MHD* Modeling of Compressed Magnetic Field Generators, in "Proceedings of the Seventh Conference on Numerical Simulation of Plasmas," Courant Institute, New York, 1975.
10. J. R. FREEMAN AND S. L. THOMPSON, Two-Dimensional *MHD* Modeling of Compressed Magnetic Field Generators, Part I: The Magnetic Field Solver, Sandia Laboratories Report SAND-75-0375, 1975.
11. S. L. THOMPSON, Improvements in the CHARTD Energy Flow-Hydrodynamic Code V: 1972/1973 Modifications, Sandia Laboratories Report SLA-73-0477, 1973.
12. W. R. SMYTHE, "Static and Dynamic Electricity," McGraw-Hill, New York, 1950.
13. J. R. FREEMAN, *Nuc. Fusion* **11** (1971), 425.
14. J. W. POUKEY, J. R. FREEMAN, AND M. REISER, *Part. Accel.* **6** (1975), 245.
15. J. P. BORIS AND D. L. BOOK, *J. Comp. Phys.* **11** (1973), 38.
16. A. R. MITCHELL, "Computational Methods in Partial Differential Equations," Wiley, London, 1969.
17. R. D. RICHTMYER AND K. W. MORTON, "Difference Methods for Initial-Value Problems," Interscience, New York, 1967.
18. E. LEE, M. FINGER, AND W. COLLINS, *JWL* Equation of State Coefficients for High Explosives, Lawrence Livermore Laboratory Report UCID-16189, 1973.
19. The experimental current values were recorded using a linear response scope. Trace reading errors are a few percent of the peak current. For L15 this is unfortunately in the same range (200 to 300 A) as the initial current. A cross comparison with more accurate current measurements in the charging circuit indicated a baseline error. All plotted currents for L15 were thus shifted by 80 A for this comparison. No corrections were used for L14 since recording errors are reduced because of the lower peak current.
20. T. J. TUCKER AND J. E. LEEMAN, *SWL* and *BWL*: Finite Element Models of Compressed Magnetic Field Current Generators, Sandia Laboratories Report SAND-75-0604, 1976.
21. M. COWAN *et al.*, Multi-Megajoule Pulsed Power Generation from a Reusable Compressed Magnetic Field Device, in "Proceedings of the International Conference on Energy Storage, Compression, and Switching," Plenum Press, New York, 1976.
22. G. YONAS *et al.*, *Nuc. Fusion* **14** (1974), 731.